

VIP Very Important Paper

Special Collection

www.batteries-supercaps.org

Chemical Substitution-Grown Lithium-Magnesium Alloy as Ion Redistributor and Surface Protector for Highly Stable Lithium-Metal Anode

Zenan Zhao,^[a, b] Mengmeng Qian,^[a, b] Jing Wang,^{*,[a, b]} Wenze Cao,^[a, b] Xianfu Qin,^[a, b] Penghui Guo,^[a, b] Shuang Hao,^[a, b] Ran Wang,^[a, b] Feng Wu,^[a, b] and Guoqiang Tan^{*,[a, b, c]}

Addressing lithium-dendrite problem caused by uneven lithium (Li) plating/stripping is crucial for improving cycle-life and safety of Li-metal batteries. Here we describe a simple chemical substitution method of $2\text{Li} + \text{Mg}(\text{PF}_6)_2 = \text{Mg} + 2\text{LiPF}_6$ to construct a highly stable Li–Mg alloy on Li metal anode. The self-grown Li–Mg alloy exhibits homogeneous β -phase bulk structure with flat and dense surface morphology. Systematic studies reveal that the obtained Li–Mg film acts as ion redistributor and surface stabilizer to protect Li metal anode by its low strain, fast conductivity, superior lithophilicity and

excellent stability. Compared to the bare Li metal, symmetric cells assembled using Li–Mg-protected Li exhibit better cycling performance with lower charge-discharge overpotential. Notably, this Li–Mg film demonstrates great potential for Li-metal batteries, it can effectively suppress Li-dendrite growth and work effectively in $\text{LiFePO}_4//\text{Li}$ and $\text{LiNi}_{0.8}\text{Co}_{0.1}\text{Mn}_{0.1}\text{O}_2//\text{Li}$ cells. This work provides a simple and effective strategy to construct Li-ion redistributor and surface protector to guard Li anodes operating in high-energy Li batteries.

Introduction

Lithium (Li) metal has exhibited huge potential in next-generation high-energy Li batteries (such as Li–S, Li–O₂ and solid-state Li batteries) owing to the low reduction potential (−3.04 V vs. standard hydrogen electrode) and extremely high theoretical capacity (3860 mAh g^{−1}).^[1] However, these Li-metal batteries have long suffered from poor cycle life, low Coulombic efficiency, and severe safety concerns caused by sharp Li-dendrites and vicious electrolyte degradation. In general, Li-dendrite growth originates from inhomogeneous Li nucleation on Li metal surface and is further exacerbated by unstable Li-electrolyte interphase properties, such as high chemical reactivity, complex ion transport paths, high polarization potential, and unbalanced local current density, etc.^[2]

Many strategies have been proposed to tackle the above problems, and tremendous efforts have been made towards

this direct. So far, a straightforward approach has been to pre-construct stable artificial protective films on Li metal, where ion and electron transport and Li nucleation can be regulated. On the basis of chemical composition, these artificial films can be classified into three categories: organic (e.g., strong and soft polymers),^[3] inorganic (e.g., carbon, silica, MoS₂, LiF, and phosphorene),^[4] and hybrids (e.g., ceramics/polymers and metal organic frameworks).^[5] Despite extensive research and great achievements in recent years, there are still some intrinsic drawbacks of this approach. Firstly, most artificial films exhibited poor electrochemical stability, either easily lithiate into new mesophases, or participate in the electrolyte's decomposition to promote a thick solid-electrolyte interface (SEI).^[6] Secondly, conventional methods (e.g., physical coating and vapor deposition) tend to build the physical protective layers, but it is difficult to form efficient electron-conduction networks due to large interfacial impedance; besides, artificial films exhibit the poor adhesion to Li metal due to the lack of stable interactions.^[7] Furthermore, the mass-processing and scalable applications are limited by harsh fabrication and high-cost with current manufacturing technologies.

To address all above technical challenges, chemical substitution strategy featuring facile and controllable synthesis offers an effective way to pre-build stable and dense artificial films. Here, we report a simple chemical method for the artificial engineering of Li metal anodes by in-situ constructing a Li–Mg alloy protector on the surface of Li metal. Previous studies have demonstrated that Li–Mg alloy has fast Li-ion diffusion and can keep largely bulk intact after delithiation.^[8] Furthermore, based on the Li–Mg alloy phase diagram, the capacity of this alloy can be tuned in a broad range while remaining phase-change free.^[9] Specifically, the obtained Li–Mg alloy layer promotes fast charge transfer and reaction

[a] Z. Zhao, M. Qian, Dr. J. Wang, W. Cao, X. Qin, P. Guo, S. Hao, Dr. R. Wang, Prof. F. Wu, Prof. G. Tan

School of Materials Science & Engineering
Beijing Institute of Technology
Beijing, 100081, PR China
E-mail: wangjingbit98@bit.edu.cn
tan123@bit.edu.cn

[b] Z. Zhao, M. Qian, Dr. J. Wang, W. Cao, X. Qin, P. Guo, S. Hao, Dr. R. Wang, Prof. F. Wu, Prof. G. Tan

Beijing Institute of Technology Chongqing Innovation Center
Chongqing, 401120, PR China

[c] Prof. G. Tan
Experimental Center of Materials Sciences and Engineering
Beijing Institute of Technology
Beijing 100081, PR China

 Supporting information for this article is available on the WWW under
<https://doi.org/10.1002/batt.202200232>

 An invited contribution to a Special Collection on IV Symposium on Advanced Energy Storage.

kinetics at the interface, thereby affording stable and homogeneous deposition of Li without dendrite growth. In addition, this Li–Mg alloy is much more inert with respect to the electrolyte than Li alone, thus reducing side reactions between Li and electrolyte. When measured in a symmetrical cell and used in a LiFePO₄//Li cell and a LiNi_{0.8}Co_{0.1}Mn_{0.1}O₂//Li cell, Li–Mg alloy shows remarkable stability, providing a promising solution for Li metal batteries.

Results and Discussion

Figure 1(a) illustrates chemical substitution mechanism of constructing Li–Mg alloy layer by the spontaneous reaction between Li and anhydrous Mg(PF₆)₂-THF solution onto Li metal surface. During the mild reaction of $2\text{Li} + \text{Mg}(\text{PF}_6)_2 = \text{Mg} + 2\text{LiPF}_6$, Li atoms on Li metal surface are easily combined with PF₆[−] anions and oxidized to LiPF₆, which are dissolved into reaction solvent, meanwhile, Mg²⁺ cations are reduced to Mg⁰ and then alloyed with the remaining Li atoms on Li metal surface to constitute Li–Mg alloy layer. The resulting Li–Mg-protected Li metal (denoted as Li/LiMg) is directly used for material and electrochemical characterizations without further treatments.

We first characterized surface structures of Li/LiMg using SEM and XRD measurements (Figure 1b–h). Bare Li foil (Figure 1b–d) was characterized as a comparison, which shows an uneven surface morphology with plenty of raised streaks under a high-magnification SEM microscope (Figure 1c). In contrast, after the design substitution, the resulting Li/LiMg foil (Figure 1e, f) displays a denser and smoother morphology than the bare Li foil. In addition, from the SEM cross-section view of Li/LiMg sample (Figure 1g), a thin-film of ~17.6 μm is observed to grow onto the bulk lithium, which is absent for the bare Li metal (Figure 1d). This finding suggests that after chemical substitution, an intact thin-film grows firmly onto Li metal surface. Notably, the obtained Li/LiMg foil looks much brighter than the bare Li foil (Figure S1). XRD pattern (Figure 1h) further reveals its crystalline structural characteristics. Obviously, the Li/LiMg foil displays four characteristic peaks at 36.19°, 51.97°, 64.98° and 76.66°, which reveals its bulk cubic center structure of the metallic Li (corresponding to the PDF#15-0401).^[10] Besides, another set of diffraction peaks appeared near above main peaks at slightly higher degree of 52.05°, 65.03°, 76.76° are found to be ascribed to the β-phase Li–Mg alloy.^[11] Thus, it can confirm that the Li–Mg alloy thin-film is substitution-grown onto Li foil surface. In general, the content of grown Li–Mg alloy is related to the reaction time, and the SEM cross-section images (Figure S2) show the thickness of grown Li–Mg alloy, where there is a logarithmic growth trend between thickness and reaction time (Figure S3). Meanwhile, the surface morphologies of Li/LiMg samples exhibit a regular evolution with the increase of reaction time (Figure S4). Unlike the bare Li foil, the surface of Li/LiMg foils immersed for 10–30 s become dense and smooth due to the uniform nucleation and growth of Li–Mg alloys. However, as the time further increases to 60 s, plenty of granular protrusions appear on the surface, which is

considered to be caused by agglomeration of precipitated Mg. Usually, when the Mg content exceeds its solubility in the alloy, the excess Mg atoms will transform from solid solution to precipitate, which is a common phenomenon of the Mg supersaturation in Mg alloys.^[12] The particle size of granular protrusions is found to increase as increasing the reaction time. By contrast, among all these samples, the sample immersed for 20 s shows the most flat and dense surface structure, which is believed to be favorable for the uniform ion nucleation and transport for Li plating/stripping.

To measure their electrochemical properties, Li/LiMg samples immersed for 10, 20, 30 and 60 s were separately assembled in symmetric cells for the galvanostatic cycling tests at a current density of 1 mA cm^{−2} with an area capacity of 1 mAh cm^{−2}. Comparatively, the 20 s sample (Figure S5) exhibits the flattest voltage-time cycling profile with the lowest voltage hysteresis among four samples, it is thus further evaluated in subsequent experiments. Figure 2(a) compares the long cycling performance of symmetric cells separately using bare Li metal and Li/LiMg. Obviously, the Li/LiMg sample exhibits a very stable cycling performance of voltage-time over 600 h with a low hysteresis voltage of less than 0.1 V, which is superior to that of the bare Li. Notably, hysteresis voltages of Li/LiMg and bare Li are almost the same at primary cycles (0–100 h), after then the hysteresis voltage of bare Li starts to increase quickly (Figure 2b, c), usually corresponding to the growth of Li-dendrites. The hysteresis voltage increases sharply to 300 mV after cycling for 380 h, and the voltage-time cycling seems to be disordered (Figure 2d). This change represents the possible micro-short circuit inside the cell, which can be attributed to the dead Li caused by continuous accumulation of Li-dendrites.^[13] Differently, the Li/LiMg exhibits excellent capability to promote uniform Li deposition and extraction, presenting the relatively stable voltage hysteresis change: 30 mV at 110–140 h, 35 mV at 210–240 h, and 45 mV at 400–440 h. EIS measurements were also carried out to verify this improved cycle stability (Figure S6). Comparatively, Li/LiMg exhibits lower resistance values with a slower increase trend than the bare Li. After 400 h cycling, the impedance of Li/LiMg is slightly increased from 13 to 22 Ω, while the impedance of bare Li is significantly increased from 18 to 78 Ω. In general, for a symmetric cell test, the low impedance indicates the fast charge-transfer and electrode dynamics, and the slowly increasing trend of impedance reflects the stable electrochemical reversibility. EIS results indicate that this Li–Mg alloy film indeed facilitates fast charge transfer and stabilizes Li/LiMg electrode surface due to its good lithophilicity and high conductivity.^[14] Therefore, Li–Mg alloy is used as an effective charge redistributor to promote fast electron and ion transport and uniform Li deposition/extraction. Cycled electrodes of symmetric cells were then characterized by SEM to verify their surface structured changes (Figure S7). Obviously, the surface of cycled bare Li becomes very rough, uneven and porous, displaying remarkable cracks and dendrites. In this case, the electrolyte can continuously penetrate into electrode bulk through these cracks, corroding fresh Li inside and depleting active materials.^[15] Comparatively, the cycled Li/LiMg displays a

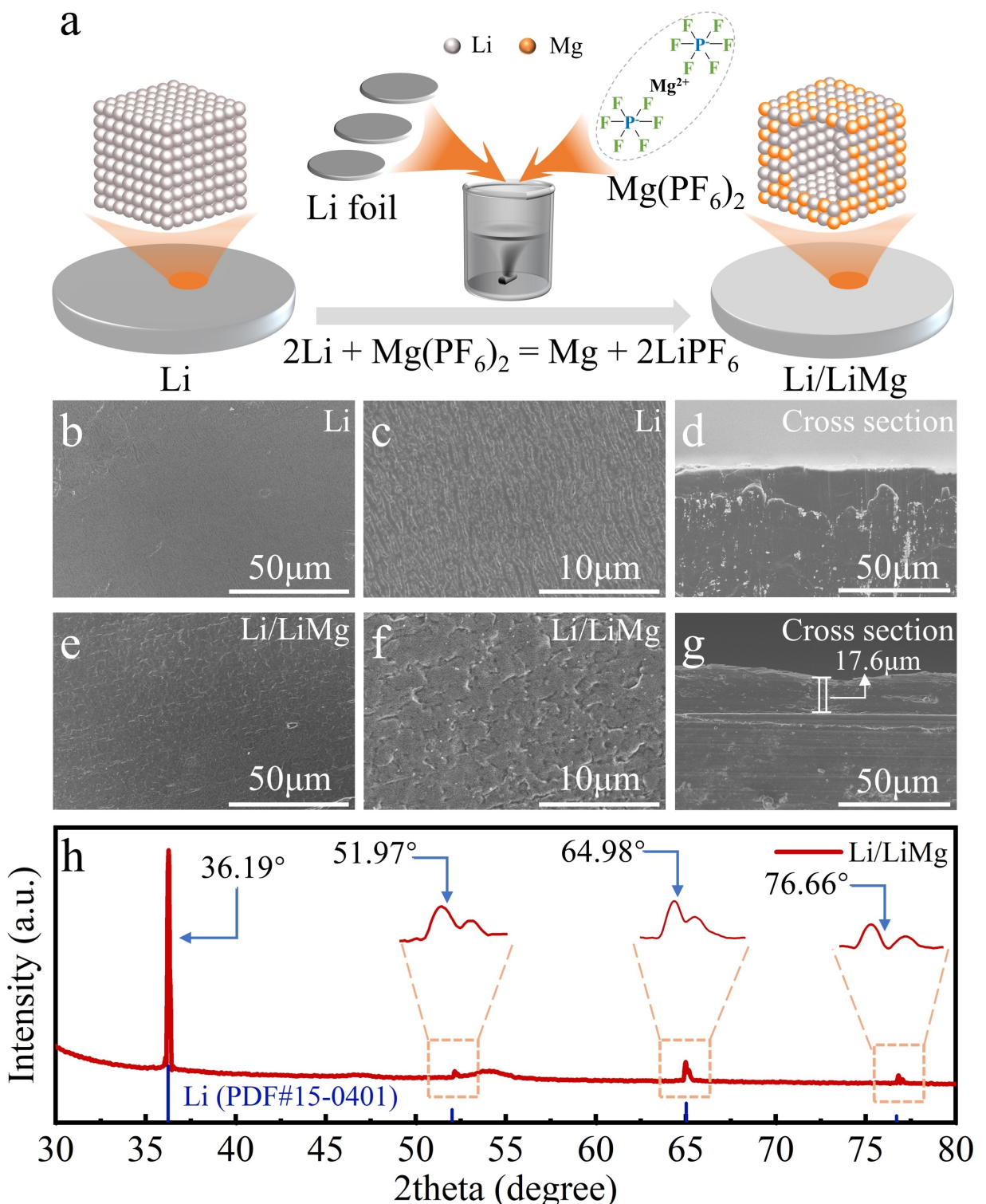


Figure 1. Material preparation and structural characterization. a) Schematic diagram of the preparation of Li–Mg alloy thin-film on Li metal surface. b, c) Surface morphology of bare Li metal. d) Cross-section morphology of bare Li metal. e, f) Surface morphology of Li/LiMg. g) Cross-section morphology of Li/LiMg. h) XRD pattern of Li/LiMg.

relatively intact, smooth and dense surface morphology without obvious Li-dendrites. After cycling for 400 h, the surface of cycled bare Li is severely damaged, with several large cracks and thick Li-dendrites (Figure 2e, f). In addition, the surface layer of bare Li is pulverized into a loose porous region with a

thickness of ~114 μm (Figure 2g). In contrast, the Li/LiMg maintains a relatively complete, flat and dense morphology (Figure 2h, i) and a loose surface layer of ~57 μm (Figure 2j). This result indicates that the self-grown Li–Mg alloy layer can resist the corrosion of Li metal by electrolyte and maintain the

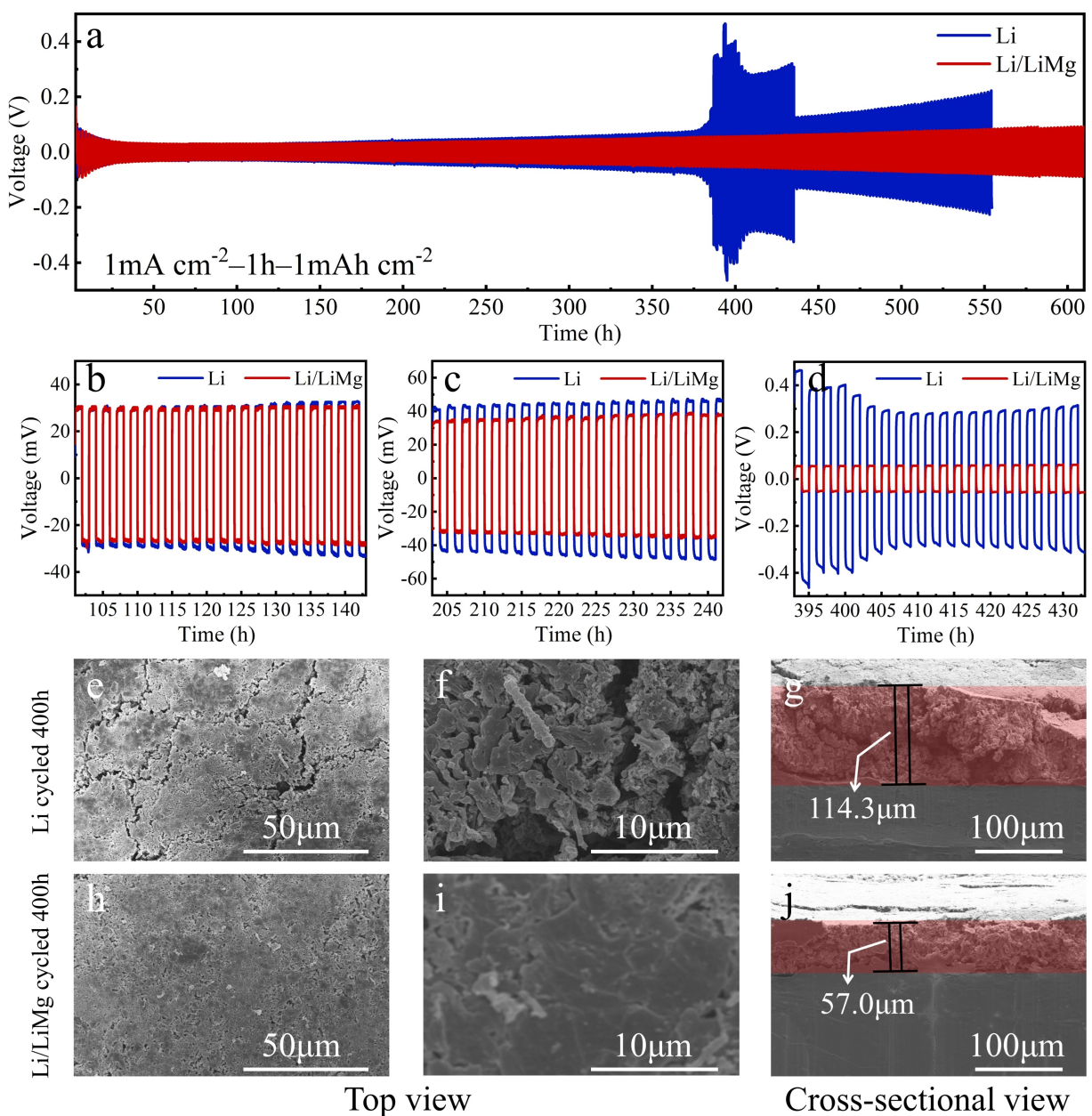


Figure 2. Cycling stability of symmetric cells and SEM characterization of cycled electrodes. a-d) Voltage-time profiles of a) 600 h cycling and b) corresponding enlarged view of 100–140 h, c) 200–240 h, and d) 390–430 h. e, f) Surface and g) cross-section morphologies of bare Li metal after 400 h cycling. h, i) Surface and j) cross-section morphologies of Li/LiMg after 400 h cycling.

surface structural integrity, acting as the surface stabilizer. More importantly, the free phase change of Li–Mg alloy can alleviate large volume change of Li during the repeated Li deposition/extraction processes.^[16]

To further evaluate the electrochemical behavior of symmetric cells of bare Li metal and Li/LiMg at high current densities with high area capacity, the galvanostatic cycling tests at different current densities (2, 4, 8 mA cm⁻²) with an area capacity of 4 mAh cm⁻² were carried out. For bare Li, its hysteresis voltage value increases quickly and becomes disordered when cycled to 175 h (Figure 3a, b). It is believed to be caused by the uneven current density distribution originating from the continuous growth and accumulation of Li-

dendrites.^[17] In contrast, the Li/LiMg maintains smooth curves with low hysteresis voltages even cycled to 200 h (Figure 3b). At a higher current density of 4 mA cm⁻², the hysteresis voltage of bare Li starts to increase after cycling only 30 h (Figure 3c), and becomes seriously disordered when cycled to 77 h (Figure 3d). In contrast, the Li/LiMg can maintain stable cycling curves with relatively low hysteresis voltages until 90 h (Figure 3d). Even at an exceedingly high current density of 8 mA cm⁻², the Li/LiMg can still maintain stable cycling for at least 30 h (Figure 3e, f). Obviously, the voltage-time profile of Li/LiMg is much smoother than that of bare Li. That is to say, at high current density with high area capacity, the Li/LiMg can also enable fast Li⁺ ions transport and uniform Li deposition/

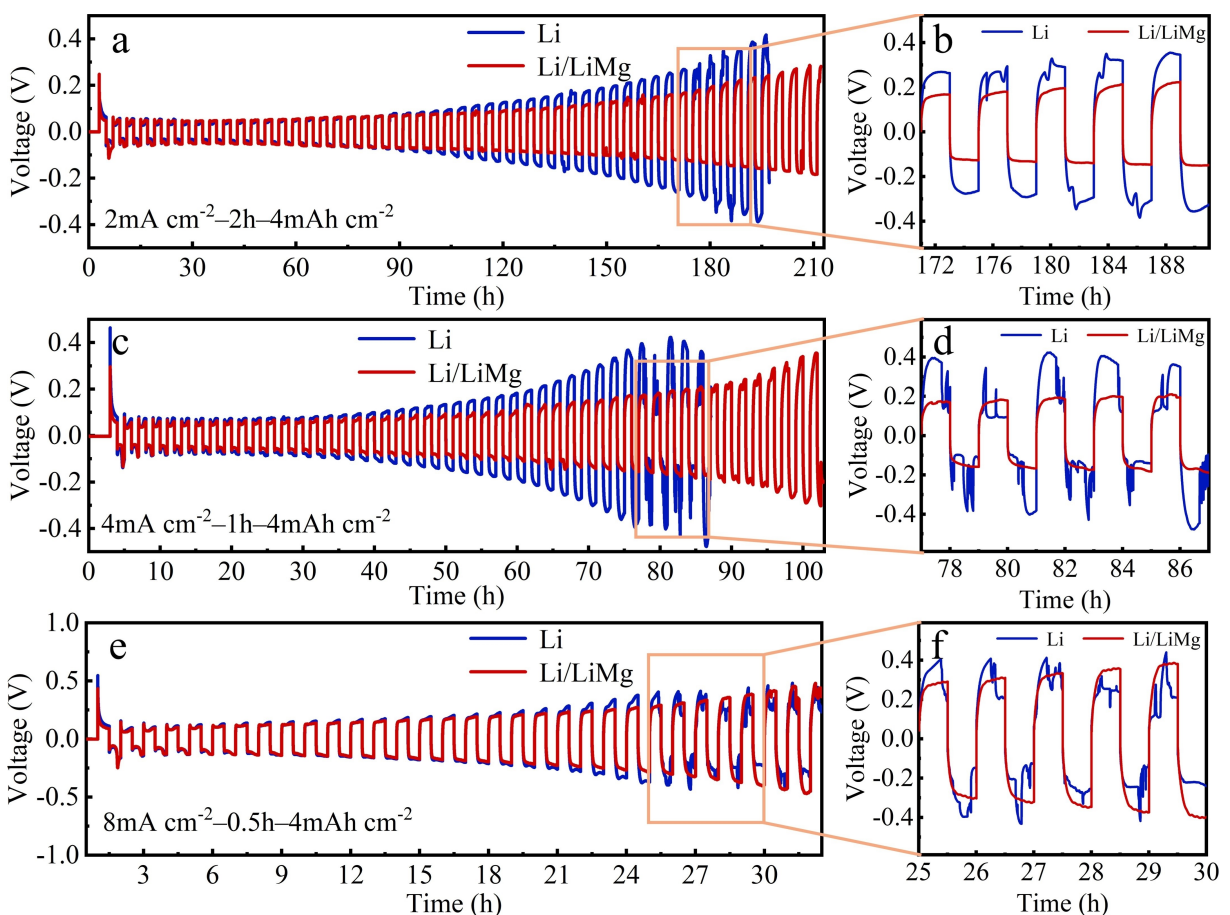


Figure 3. Electrochemical performance of symmetric cells using bare Li metal and Li/LiMg as electrodes, respectively. a) Voltage-time profile of symmetric cells at a current density of 2 mA cm^{-2} with an area capacity of 4 mAh cm^{-2} . b) Voltage-time profile of (a) in an enlarged view of 170–190 h. c) Voltage-time profile of symmetric cells at a current density of 4 mA cm^{-2} with an area capacity of 4 mAh cm^{-2} . d) Voltage-time profile of (c) in an enlarged view of 79–87 h. e) Voltage-time profile of symmetric cells at a current density of 8 mA cm^{-2} with an area capacity of 4 mAh cm^{-2} . f) Voltage-time profile of (e) in an enlarged view of 25–30 h.

extraction. Briefly, this homogeneous Li–Mg alloy film ensures the stable long-cycling of symmetric cells.

To explore the rate cycling performance of Li/LiMg, symmetric cells were evaluated by galvanostatic cycling at an area capacity of 1 mAh cm^{-2} using an increasing current density. In Figure 4(a), the Li/LiMg symmetric cell delivers a steady cycling curve with relatively low hysteresis voltages of 30, 41, 53, 80, 160, and 18 mV at 1, 2, 3, 5, 10, and 1 mA cm^{-2} , respectively, which are much lower than those of bare Li symmetric cell (40, 55, 71, 120, 230 and 27 mV). This indicates that Li/LiMg electrode exhibits a fast charge-transfer capability. In Figure 4(b), EIS measurements were performed to evaluate their interfacial resistances after rate cycles. Comparatively, the Li/LiMg exhibits a lower SEI resistance (R_{sei}) of 2.2Ω and a lower charge transfer resistance (R_{ct}) of 7.2Ω than those of bare Li ($R_{\text{sei}} = 3.2 \Omega$ and $R_{\text{ct}} = 13.0 \Omega$), this result suggests that the Li–Mg alloy enables fast electrochemical reaction kinetics.^[18] To verify its surface stability, SEM measurements were also performed to observe the surface morphologies of cycled electrodes. For the bare Li, in Figure 4(c), large pulverized cracks and plenty of dead Li-dendrites are observed on cycled electrode surface. Differently, the cycled Li/LiMg maintains

complete and dense surface without obvious cracks and pores (Figure 4d), indicating that the Li/LiMg has advantages of promoting uniform Li deposition to inhibit the Li-dendrite growth. More notably, Li–Mg alloy film serves as surface stabilizer that protects electrode against the electrolyte corrosion, forming a stable electrode/electrolyte interface.^[9] Furthermore, we evaluated the Coulombic efficiency of Li–Mg alloy by using an asymmetric Cu/LiMg//Li cell. For comparison, an asymmetric Cu//Li cell was measured under the same condition. Figure 4(e) illustrates the applied Li plating/stripping protocol for both Cu/LiMg//Li and Cu//Li cells. In Figure 4(f), Cu/LiMg//Li cell shows a relatively steady voltage hysteresis over 20 cycles, where the final stripping is performed at 1 mA cm^{-2} to 1 V. And the obtained Q_s was 4.45 mAh cm^{-2} . According to Equation (1):^[19]

$$\text{CE}_{\text{avg}} = \frac{nQ_c + Q_s}{nQ_c + Q_T} \quad (1)$$

The calculated average Coulombic efficiency of Cu/LiMg//Li cell is 97.8%. By contrast, as the cycle number reaches to 16 cycles, the voltage hysteresis of Cu//Li cell increases sharply

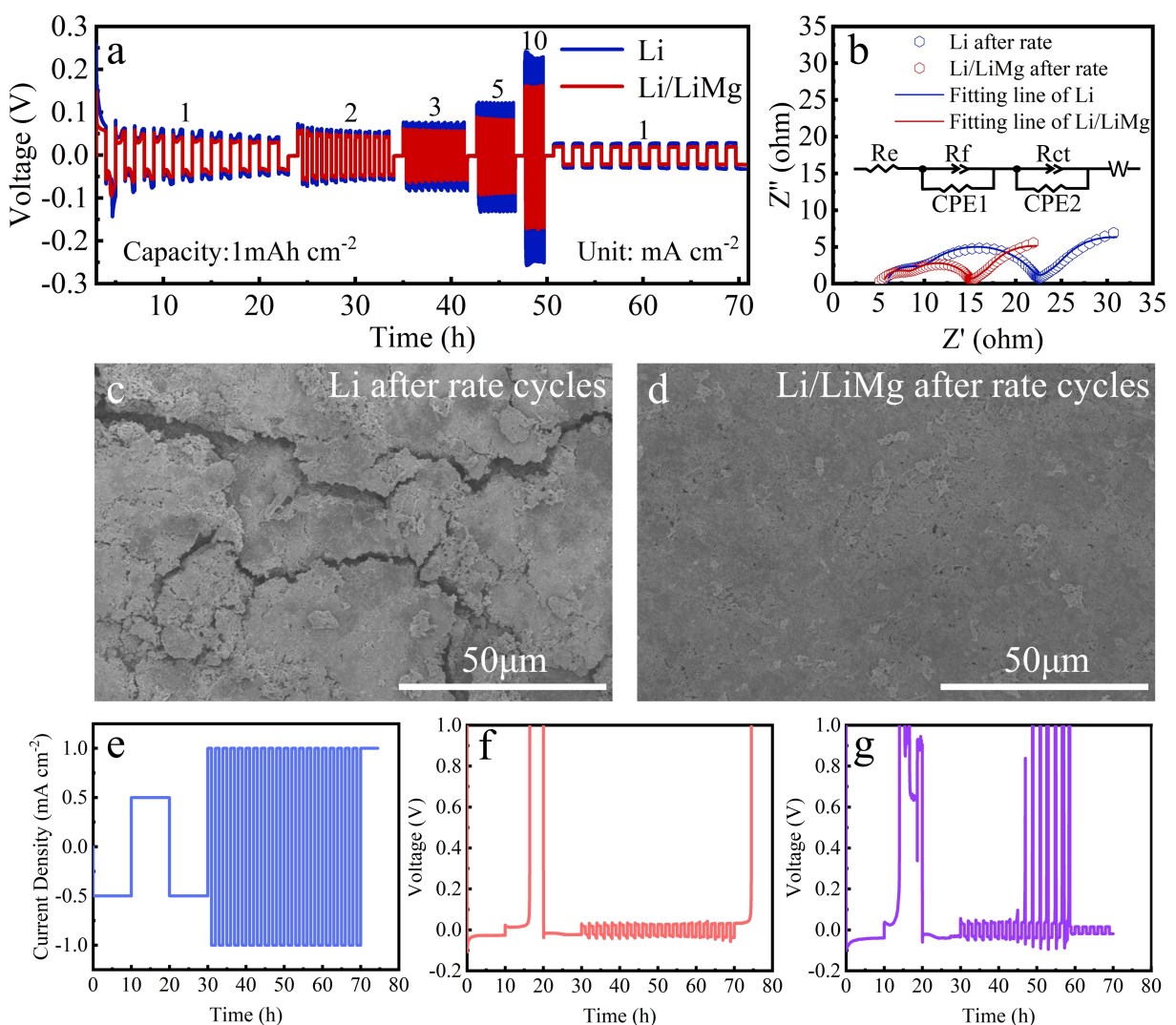


Figure 4. a) Rate performance of symmetric cells using bare Li metal and Li/LiMg electrodes at the different current densities (1, 2, 3, 5, 10, and 1 mA cm⁻²) with the area capacity of 1 mAh cm⁻². b) EIS profiles of symmetric cells after rate cycles. c, d) Surface morphologies of c) Li and d) Li/LiMg electrodes after rate cycles. e) The constant current protocol for measuring Coulombic efficiency of Cu/LiMg//Li and Cu//Li cells. f, g) Voltage versus time plots of f) Cu/LiMg//Li and g) Cu//Li cells.

and then rapidly drops to a low value, indicating an internal short circuit phenomenon occurring in the Cu//Li cell (Figure 4g). This result further confirms that Li–Mg alloy layer can promote fast charge transfer and reaction kinetics.

Based on the above comprehensive characterizations and measurements, we demonstrate a chemical substitution-grown artificial Li–Mg alloy film, which can act as ion redistributor and surface protector for Li metal anodes. The resulting Li/LiMg electrode exhibits unique structural and electrochemical properties, including high lithophilicity, free phase change, fast charge transfer, and good electrochemical stability. This rational artificial engineering of the Li–Mg alloy film is expected to achieve excellent electrochemical performance in Li metal batteries.

To verify the application of Li/LiMg anode in Li batteries, cells paired with LFP cathodes were measured to explore their electrochemical performance. In Figure 5(a), both Li/LiMg and bare Li anodes were separately paired with LFP cathodes for

long-cycling tests at 1 C rate ($1\text{C} = 170\text{ mAh g}^{-1}$) in the voltage range of 2.5–4.1 V. The LFP//Li/LiMg cell delivers a high discharge capacity of 121.4 mAh g^{-1} with a high initial Coulombic efficiency of 98.52%, and maintains a good capacity retention of 90.2% after 450 cycles. In contrast, the LFP//Li cell shows a fast capacity fading after 250 cycles, which is always caused by the accumulation of dead Li and the consumption of electrolytes. In Figure 5(b), the rate performance of LFP//Li and LFP//Li/LiMg cells were also tested at gradually increasing current rates. Comparatively, LFP//Li/LiMg cell shows a better rate capability, offering the specific discharge capacities of 145.7, 132.9, 120.5, 106.6 and 86.5 mAh g^{-1} at current rates of 0.2, 0.5, 1.0, 2.0 and 5.0 C, which are higher than that of LFP//Li cell (132.9, 123.2, 107.7, 96.6, 76.3 mAh g^{-1}). After that, EIS tests were carried out to compare their resistance changes for further exploring the interfacial stability of electrodes. In Figure 5(c), the cycled LFP//Li/LiMg cell shows a much lower cell resistance of 129.1Ω than the cycled LFP//Li cell (855.4Ω).

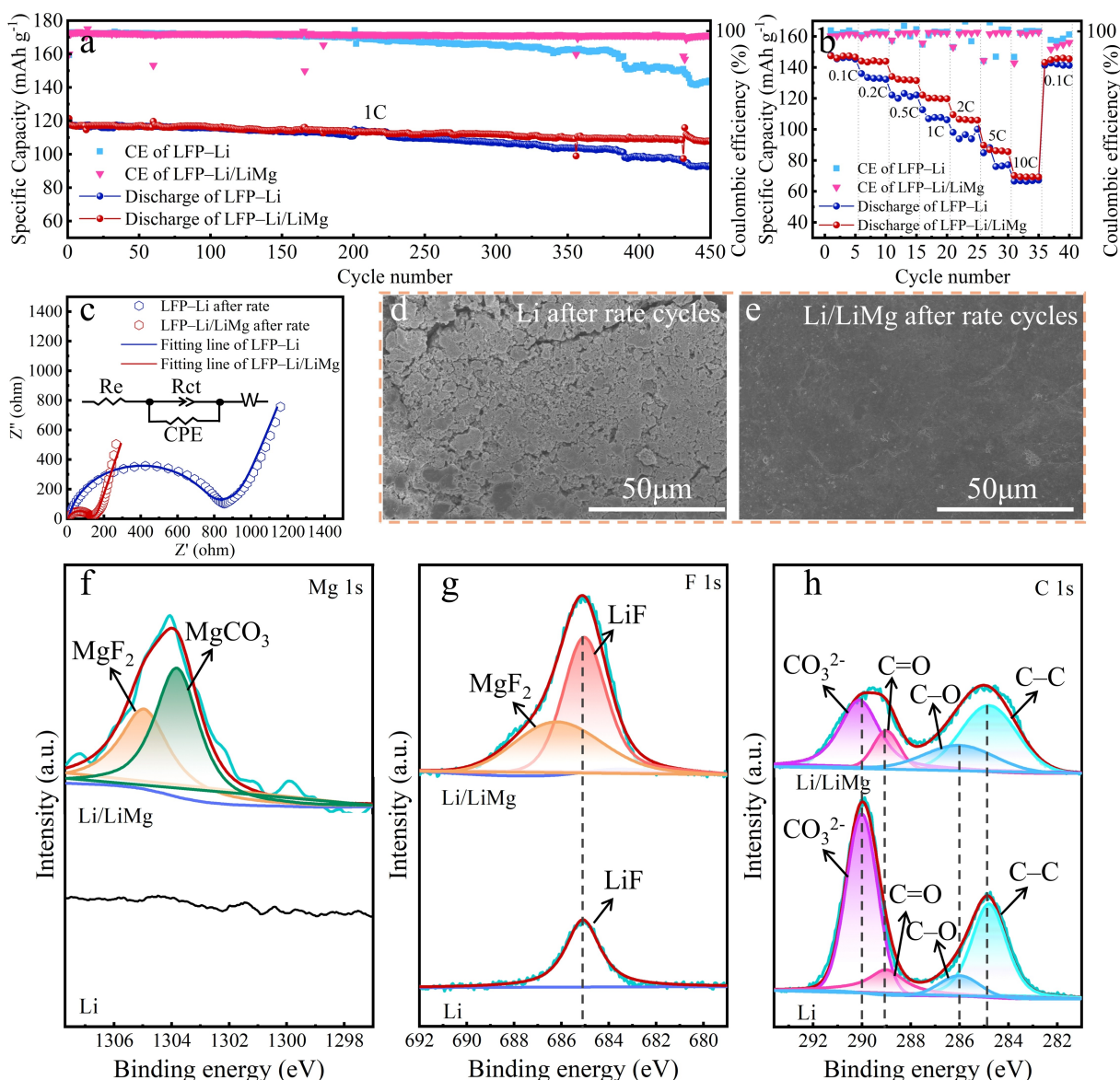


Figure 5. a) Long-cycling performance of LFP//Li and LFP//Li/LiMg cells at 1.0 C. b) Rate performance of LFP//Li and LFP//Li/LiMg cells. c) EIS profiles of LFP//Li and LFP//Li/LiMg cells after rate cycles. d, e) Surface morphologies of d) bare Li metal and e) Li/LiMg anodes after rate cycles. f–h) XPS spectrum of f) Mg 1s, g) F 1s and h) C 1s for cycled bare Li metal and Li/LiMg anodes.

Since two cells use the same cathode and electrolyte, the difference in cell resistance is more related to interface characteristics of anodes. The lower resistance of LFP//Li/LiMg cell thus demonstrates that the more favorable interfacial properties of Li/LiMg rather than the bare Li. In addition, the anode morphologies after rate cycles were characterized by SEM to evaluate their structured integrity. In Figure 5(d), the cycled bare Li anode shows rough electrode surface with several cracks and plenty of pulverized dead Li (Figure S8), indicating that the cycled Li is severely damaged by electrolyte corrosion. In contrast, in Figure 5(e), the cycled Li/LiMg anode is still smooth and dense, without obvious cracks and spikes. As in the analysis of the results in the symmetrical cell above, during cycling in LFP//Li/LiMg cell, the Li/LiMg anode can achieve uniform Li deposition/extraction on the Li–Mg alloy

film without Li-dendrites. The dense and flat film morphology facilitate rapid Li⁺ ion transport and charge transfer, which thus enables low interfacial impedance in the EIS profile. The low interfacial impedance is believed to help cells maintain stable long-cycle performance. These results indicate that the self-grown Li–Mg alloy film is beneficial to promote uniform Li plating/stripping and protect the anode from the electrolyte. XPS spectra further reveal surface chemical compositions of cycled Li/LiMg and bare Li anodes. All samples were sputtered by Ar-ion beam for 200 s to remove their surface contaminants. As shown in Figure 5(f), peaks at 1303.8 eV and 1304.95 eV correspond to Mg 1s of MgCO₃ and MgF₂, respectively.^[20] This finding confirms that Mg²⁺ participates into the formation of SEI. Note that LiF is a key component to stabilize anode interface of Li metal.^[21] In the one hand, it can decrease the

surface reactivity to improve interface stability;^[22] on the other hand, it can reduce the surface energy to suppress Li-dendrite growth.^[23] Similarly, we believe that MgF₂ may have the same function. In Figure 5(g), the cycled Li anode exhibits a sharp peak at 685.1 eV assigned to LiF.^[24] Differently, except a main peak of LiF, the cycled Li/LiMg anode has a satellite peak at 686.3 eV assigned to MgF₂.^[25] That is to say, both LiF and MgF₂ are main components of SEI for the cycled Li/LiMg anode. Usually, the MgF₂ with high lithophilicity can provide well-distributed active sites, which is beneficial for the smooth SEI formation without Li-dendrites.^[26] In addition, in Figure 5(h), the C 1s XPS spectra show a strong CO₃²⁻ peak at 290.0 eV for the cycled Li anode, but a relatively weak CO₃²⁻ peak for the cycled Li/LiMg anode.^[27] Since the CO₃²⁻ species always come from the decomposition of electrolyte, it can conclude that the Li–Mg alloy is helpful to suppress the decomposition of electrolyte and can improve the electrochemical stability of Li/LiMg anode. Furthermore, to better verify the action of Li–Mg alloy for SEI formation and regulation, XPS measurements for the original Li/LiMg and the first cycled Li/LiMg anodes were performed for comparison (Figure S9). It was found that the Li–Mg alloy can maintain its bulk structure after the first cycle, and the formed SEI is mainly composed of LiF, MgF₂, Li₂CO₃, MgCO₃ and alkyl carbonates. Note that the intensity of CO₃²⁻ species on Li/LiMg anode is lower than that on bare Li anode. This finding reveals that the self-grown Li–Mg alloy can tune the chemical compositions of SEI on the anode surface. In briefly, the Li–Mg film promotes the formation of a robust SEI with multifunctional composition, which achieves a stable anode interface. As

a result, the LFP//Li/LiMg cell enables excellent electrochemical performance.

Furthermore, cells paired with NCM811 cathode were measured to verify its application in high-energy Li batteries. In Figure 6(a), after three cycles of activation at 0.1 C (1 C = 190 mAh g⁻¹), the discharge capacity of NCM811//Li/LiMg cell is 197.7 mAh g⁻¹, it can maintain at 105.2 mAh g⁻¹ after 500 cycles at 1 C rate, with the average Coulombic efficiency remains at 99.56%. Comparatively, all the performance of NCM811//Li/LiMg cell are superior to that of NCM811//Li cell. In Figure 6(b), NCM811//Li/LiMg cell delivers high discharge capacities of 213.6, 205.9, 195.3, 185.6, 172.5 and 156.7 mAh g⁻¹ at current rates of 0.2, 0.5, 1.0, 2.0, 5.0 and 10.0 C, respectively, while NCM811//Li cell delivers the relatively low capacities of 209.1, 197.6, 186.1, 174.3, 156.5 and 137.7 mAh g⁻¹ at the same step-by-step current rates, respectively. The interface stability after rate cycles was also evaluated by EIS (Figure S10). Comparatively, the R_{ct} of NCM811//Li/LiMg is much lower than that of NCM811//Li. This is consistent with the previous conclusion that Li–Mg alloy facilitates rapid Li⁺ ion transport and charge transfer. The electrode morphologies after rate cycles of both anodes and cathodes were evaluated using SEM to explore their structured stability. The cycled Li anode of NCM811//Li cell seems to be severely damaged, with plenty of pulverized cracks (Figure 6c) and dendrites (Figure 6d) on the electrode surface. In contrast, the cycled Li/LiMg anode of NCM811//Li/LiMg cell seems to be smooth and intact (Figure 6e), presenting a flat and dense surface morphology (Figure 6f), which is consistent with the cycled anode morphology of LFP//Li/LiMg cell. This finding proves that the Li–Mg alloy actually protect Li

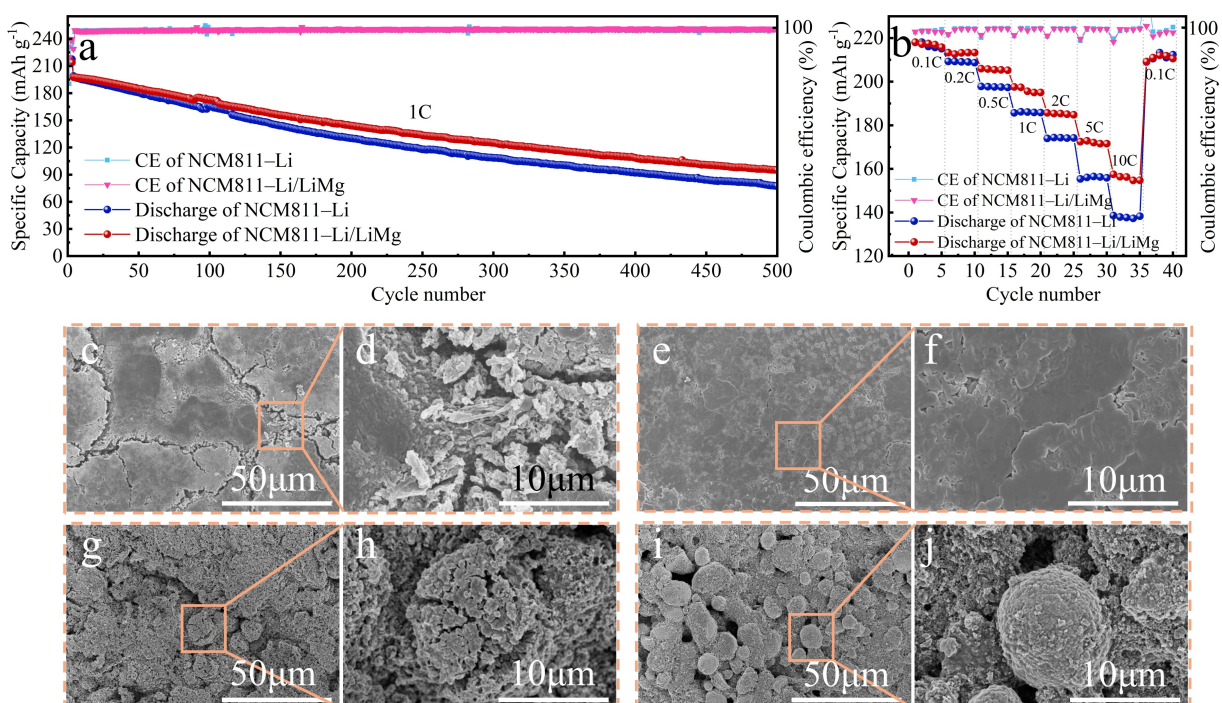


Figure 6. a) Long-cycling performance of NCM811//Li and NCM811//Li/LiMg cells at 1.0 C. b) Rate performance of NCM811//Li and NCM811//Li/LiMg cells. c-f) Surface morphologies of cycled c, d) Li metal and e, f) Li/LiMg anodes after rate cycles. g-j) Surface morphologies of cycled NCM811 cathodes in g, h) NCM811//Li and i, j) NCM811//Li/LiMg cells after rate cycles.

anode and enable uniform Li plating/stripping during electrochemical reactions, acting as anode surface stabilizer and ion redistributor. More notably, the cycled cathode morphology of NCM811//Li cell seems to be severely damaged in a large area (Figure 6(g)). In the high-magnification SEM image (Figure 6h), huge cracks appear in NCM811 sphere, indicating the seriously destroyed structure. In contrast, the cycled cathode of NCM811//Li/LiMg cell remains an intact sphere (Figure 6i) without obvious cracks (Figure 6j). Generally, the cracks of spherical NCM811 may be caused by the erosion of HF, which comes from the decomposition of electrolyte, especially the decomposition of LiPF₆ during long cycling.^[28] Furthermore, it should be noted that the inhomogeneous electrode microstructure and strain distribution lead to local current density imbalance and high interfacial impedance, which in turn lead to further degradation of electrode structure.^[29] Collectively, these drawbacks are the main reasons for the decline of electrochemical performance. Li–Mg alloy film is designed to alleviate these drawbacks, the XPS analysis has indicated that the SEI film on Li/LiMg anode is rich in LiF and MgF₂, while the content of fluorine species on NCM811 cathode is accordingly reduced. As a result, the corrosion from HF to the NCM811 is alleviated. In addition, since the standard electrode potential of Li (−3.04 V vs. H₂) is lower than that of Mg (−2.69 V vs. H₂),^[30] Li⁺ is preferentially extracted from Li–Mg alloy over Mg, the influence of Mg ions on the cathode can be ignored. That is to say, the cathode and anode with intact structure ensures superior electrochemical performance of NCM811//Li/LiMg cell. Briefly, Li–Mg alloy film can not only suppress the Li-dendrite growth, but also relieve the HF corrosion to NCM811. These results demonstrate that the Li–Mg alloy film on Li anode is an excellent Li-ion redistributor and surface protector, which enables the remarkable improvement of electrochemical performance in high-energy Li metal batteries.

Conclusion

In summary, we developed a simple chemical substitution method of $2\text{Li} + \text{Mg}(\text{PF}_6)_2 = \text{Mg} + 2\text{LiPF}_6$ to construct a highly stable Li–Mg alloy thin-film onto Li metal anode as ion redistributor and surface protector. Typically, this self-grown Li–Mg alloy thin-film has a homogenous β-phase bulk structure with flat and dense surface, and the resulting Li–Mg-protected Li anode has been demonstrated to exhibit promising electrochemical performance in Li-metal batteries. It can suppress dendrite growth and work effectively in LFP//Li/LiMg and NCM811//Li/LiMg cells. Notably, LFP//Li/LiMg cell maintains a high capacity retention of 90.5% for 450 cycles at 1.0 C, and NCM811//Li/LiMg cell realizes a steady cycle-life over 500 cycles. This alloy artificial design overcomes major constraints associated with traditional Li anode protection strategies, efficiently addressing Li-dendrite issues. The unique construction mechanism of chemical substitution may change the design paradigm of high-performance metal electrodes. Furthermore, this facile and efficient fabrication method enables

the alloy-protected Li anode to be mass-produced and scalable for high-energy Li-metal batteries.

Experimental Section

Material fabrication Commercially available magnesium hexafluorophosphate ($\text{Mg}(\text{PF}_6)_2$, 98%, Viti) was completely dissolved into the tetrahydrofuran (THF, 99.9%, Aladdin) solvent under stirring for 16 h to prepare a 0.1 M magnesium salt solution. After that Li foils were immersed into $\text{Mg}(\text{PF}_6)_2$ solution for different resting times. The Li–Mg alloy thin-films were substitution-grown onto Li metal surface. Finally, the obtained Li/LiMg foils were washed with THF solvent and dried in a vacuum chamber for 12 h. The experiments with different immersion times (10 s, 20 s, 30 s, 60 s, 5 min, 10 min, 30 min and 60 min) were performed separately. All operations were carried out in an Ar-filled glove-box with H_2O and O_2 contents below 0.01 ppm.

Material characterization All samples were stored and fabricated in an Ar-filled glove-box. Special precautions were taken during material characterizations to prevent the moisture and air contamination of samples. Electrode morphologies were examined on a Hitachi S-4800 scanning electron microscope (SEM). Crystalline structures were identified using a Rigaku Ultima IV X-ray diffraction (XRD) with a Cu-Kα radiation. Chemical compositions were determined using a Thermo Scientific Escalab 250Xi X-ray photoelectron spectroscopy (XPS) analysis system.

Electrochemical measurements To evaluate the electrochemical performance of bare Li and Li/LiMg anodes, symmetric cells of Li and Li/LiMg were separately assembled using 2032 coin-type cells. To further evaluate the Coulombic efficiency, electrochemical measurements of Cu//Li and Cu//LiMg//Li asymmetric cells were performed using 2025 coin-type cells. The Li–Mg alloy layer was constructed on a Cu foil with a fixed areal capacity of 5 mAh cm^{−2} by Li pre-depositing. The control cell used Cu foil as the working electrode and bare Li foil as the counter electrode. For the calculation of Coulombic efficiency, 5 mAh cm^{−2} capacity was used for Li plating and then the Li was fully stripped to 1 V prior to depositing Li reservoir ($Q_T = 5 \text{ mAh cm}^{-2}$) at 0.5 mAh cm^{−2} and cycling ($Q_C = 1 \text{ mAh cm}^{-2}$) for specified cycles at a current density of 1 mA cm^{−2}. The final stripping is performed at 1 mA cm^{−2} to 1 V. To test the electrochemical performance of Li metal cells, the bare Li and Li/LiMg were used as anodes, and LiFePO₄ (LFP) and LiNi_{0.8}Co_{0.1}Mn_{0.1}O₂ (NCM811) were used as cathodes, respectively. Cathodes were prepared by pasting a mixture of 80 wt% LFP or NCM811, 10 wt% acetylene black and 10 wt% poly(vinylidene fluoride) on aluminum foils. The obtained electrodes were finally calendared into a thickness of ~125 μm with a mass loading of ~7.0 mg cm^{−2}, and the calculated areal capacity of LFP and NCM811 cathodes was ~1.2 and 1.4 mAh cm^{−2}, respectively. 60 μL electrolyte (1 M LiPF₆ into 1 L ethylene carbonate (EC) + ethyl methyl carbonate (EMC) + dimethyl carbonate (DMC) (1:1:1 in volume)) was added to each cell. The separator was Celgard 2400. Cells were assembled in an Ar-filled glove-box and then aged for 24 h before electrochemical tests. Electrochemical impedance spectroscopy (EIS) tests were carried out on a CHI 660D electrochemical workstation in a frequency range of 0.1 to 100 kHz. Galvanostatic charge-discharge tests were performed on a Land CT2001A tester. The specific capacity of cells was calculated based on the mass loading of LFP or NCM811.

Acknowledgements

The authors acknowledge financial support from National Natural Science Foundation of China (22075026, 52102088). R.W. acknowledges financial support from China Postdoctoral Science Foundation (2021M690382). G.T. acknowledges financial support from Teli Fellowship from Beijing Institute of Technology, and facility support from the Analysis & Testing Center, and Experimental Center of Materials Sciences & Engineering at Beijing Institute of Technology.

Conflict of Interest

The authors declare no conflict of interest.

Data Availability Statement

The data that support the findings of this study are available in the supplementary material of this article.

Keywords: lithium anode • lithium-magnesium alloy • lithium-metal battery • ion redistributor • surface protector

- [1] a) C.-Z. Zhao, P.-Y. Chen, R. Zhang, X. Chen, B.-Q. Li, X.-Q. Zhang, X.-B. Cheng, Q. Zhang, *Sci. Adv.* **2018**, *4*, 3446; b) D. Lin, Y. Liu, Y. Cui, *Nat. Nanotechnol.* **2017**, *12*, 194–206; c) X. Shen, X.-Q. Zhang, F. Ding, J.-Q. Huang, R. Xu, X. Chen, C. Yan, F.-Y. Su, C.-M. Chen, X. Liu, Q. Zhang, *Energy Mater. Adv.* **2021**, *2021*, 1205324.
- [2] a) Y. Sun, H. W. Lee, G. Zheng, Z. W. Seh, J. Sun, Y. Li, Y. Cui, *Nano Lett.* **2016**, *16*, 1497–501; b) C. Yan, Y. X. Yao, X. Chen, X. B. Cheng, X. Q. Zhang, J. Q. Huang, Q. Zhang, *Angew. Chem. Int. Ed.* **2018**, *57*, 14055–14059; *Angew. Chem.* **2018**, *130*, 14251–14255; c) J. Zheng, R. Garcia-Mendez, L. A. Archer, *ACS Nano* **2021**, *15*, 19014–19025; d) X. B. Cheng, R. Zhang, C. Z. Zhao, Q. Zhang, *Chem. Rev.* **2017**, *117*, 10403–10473; e) J. Z. Lee, T. A. Wynn, M. A. Schroeder, J. Alvarado, X. Wang, K. Xu, Y. S. Meng, *ACS Energy Lett.* **2019**, *4*, 489–493.
- [3] a) J. Lopez, A. Pei, J. Y. Oh, G. N. Wang, Y. Cui, Z. Bao, *J. Am. Chem. Soc.* **2018**, *140*, 11735–11744; b) J. Song, H. Lee, M.-J. Choo, J.-K. Park, H.-T. Kim, *Sci. Rep.* **2015**, *5*, 14458; c) J. Luo, C. C. Fang, N. L. Wu, *Adv. Energy Mater.* **2018**, *8*, 1701482.
- [4] a) S. Huang, L. Tang, H. S. Najafabadi, S. Chen, Z. Ren, *Nano Energy* **2017**, *38*, 504–509; b) C. Wu, H. Huang, W. Lu, Z. Wei, X. Ni, F. Sun, P. Qing, Z. Liu, J. Ma, W. Wei, L. Chen, C. Yan, L. Mai, *Adv. Sci.* **2020**, *7*, 1902643; c) E. Cha, M. D. Patel, J. Park, J. Hwang, V. Prasad, K. Cho, W. Choi, *Nat. Nanotechnol.* **2018**, *13*, 337–344; d) L. Fan, H. L. Zhuang, L. Gao, Y. Lu, L. A. Archer, *J. Mater. Chem. A.* **2017**, *5*, 3483–3492.
- [5] a) G. Jiang, K. Li, F. Yu, X. Li, J. Mao, W. Jiang, F. Sun, B. Dai, Y. Li, *Adv. Energy Mater.* **2020**, *11*, 2003496; b) R. Xu, X.-Q. Zhang, X.-B. Cheng, H.-J. Peng, C.-Z. Zhao, C. Yan, J.-Q. Huang, *Adv. Funct. Mater.* **2018**, *28*, 1705838.
- [6] a) S. Gao, F. Sun, N. Liu, H. Yang, P.-F. Cao, *Mater. Today* **2020**, *40*, 140–159; b) L. Qi, Z. Wu, B. Zhao, B. Liu, W. Wang, H. Pei, Y. Dong, S. Zhang, Z. Yang, L. Qu, W. Zhang, *Chem. Eur. J.* **2020**, *26*, 4193–4203.
- [7] a) R. Xu, X.-B. Cheng, C. Yan, X.-Q. Zhang, Y. Xiao, C.-Z. Zhao, J.-Q. Huang, Q. Zhang, *Matter* **2019**, *1*, 317–344; b) F. Liu, Q. Xiao, H. B. Wu, L. Shen, D. Xu, M. Cai, Y. Lu, *Adv. Energy Mater.* **2018**, *8*, 1701744; c) Q. Jin, X. Zhang, H. Gao, L. Li, Z. Zhang, *J. Mater. Chem. A* **2020**, *8*, 8979–8988.
- [8] a) Z. Shi, M. Liu, D. Naik, J. L. Gole, *J. Power Sources* **2001**, *92*, 70–80; b) T. J. Richardson, G. Y. Chen, *J. Power Sources* **2007**, *174*, 810–812.
- [9] L. L. Kong, L. Wang, Z. C. Ni, S. Liu, G. R. Li, X. P. Gao, *Adv. Funct. Mater.* **2019**, *29*, 1808756.
- [10] M. Jagannathan, K. S. R. Chandran, *J. Electrochem. Soc.* **2013**, *160*, A1922–A1926.
- [11] a) A. A. Nayeb-Hashemi, J. B. Clark, A. D. Pelton, *Bull. Alloy Phase Diagrams* **1984**, *5*, 365–374; b) Y. Miao, K. Xie, Q. Xiang, Z. Xiong, D. Zhang, L. Duan, *Phys. Status Solidi A* **2016**, *213*, 3245–3249; c) B. R. Lanning, R. Wei, *Surf. Coat. Technol.* **2004**, *186*, 314–319.
- [12] a) H. Yukawa, Y. Murata, M. Morinaga, Y. Takahashi, H. Yoshida, *Acta Metall. Mater.* **1995**, *43*, 681–688; b) M. Madanat, M. Liu, J. Banhart, *Acta Mater.* **2018**, *159*, 163–172; c) C. Shuai, C. He, G. Qian, A. Min, Y. Deng, W. Yang, X. Zang, *Composites Part B* **2021**, *207*, 108564.
- [13] Y. Xiang, M. Tao, G. Zhong, Z. Liang, G. Zheng, X. Huang, X. Liu, Y. Jin, N. Xu, M. Armand, J.-G. Zhang, K. Xu, R. Fu, Y. Yang, *Sci. Adv.* **2021**, *7*, eabj3423.
- [14] S. Zhang, G. Yang, Z. Liu, S. Weng, X. Li, X. Wang, Y. Gao, Z. Wang, L. Chen, *ACS Energy Lett.* **2021**, *6*, 4118–4126.
- [15] H. Liu, X.-B. Cheng, J.-Q. Huang, S. Kaskel, S. Chou, H. S. Park, Q. Zhang, *ACS Materials Lett.* **2019**, *1*, 217–229.
- [16] R. A. Guidotti, P. J. Masset, *J. Power Sources* **2008**, *183*, 388–398.
- [17] W. Yan, X. Gao, X. Jin, S. Liang, X. Xiong, Z. Liu, Z. Wang, Y. Chen, L. Fu, Y. Zhang, Y. Zhu, Y. Wu, *ACS Appl. Mater. Interfaces* **2021**, *13*, 14258–14266.
- [18] X. Liang, Q. Pang, I. R. Kochetkov, M. S. Sempere, H. Huang, X. Sun, L. F. Nazar, *Nat. Energy* **2017**, *2*, 17119.
- [19] B. D. Adams, J. Zheng, X. Ren, W. Xu, J.-G. Zhang, *Adv. Energy Mater.* **2017**, *8*, 1702097.
- [20] a) Y. Liu, J. Zhang, S. Wang, S. Jiang, Q. Liu, X. Li, Z. Wu, G. Yu, *ACS Appl. Mater. Interfaces* **2015**, *7*, 26643–26648; b) Z. H. Xie, D. Li, Z. Skeete, A. Sharma, C. J. Zhong, *ACS Appl. Mater. Interfaces* **2017**, *9*, 36247–36260.
- [21] a) Y. Wang, F. Liu, G. Fan, X. Qiu, J. Liu, Y. Yan, K. Zhang, F. Cheng, J. Chen, *J. Am. Chem. Soc.* **2021**, *143*, 2829–2837; b) C. Yan, X. B. Cheng, Y. X. Yao, X. Shen, B. Q. Li, W. J. Li, R. Zhang, J. Q. Huang, H. Li, Q. Zhang, *Adv. Mater.* **2018**, *30*, 1804461; c) A. Hu, W. Chen, X. Du, Y. Hu, T. Lei, H. Wang, L. Xue, Y. Li, H. Sun, Y. Yan, J. Long, C. Shu, J. Zhu, B. Li, X. Wang, J. Xiong, *Energy Environ. Sci.* **2021**, *14*, 4115–4124; d) F. Li, Y. H. Tan, Y. C. Yin, T. W. Zhang, L. L. Lu, Y. H. Song, T. Tian, B. Shen, Z. X. Zhu, H. B. Yao, *Chem. Sci.* **2019**, *10*, 9735–9739.
- [22] S. D. Ware, C. J. Hansen, J. P. Jones, J. Hennessy, R. V. Bugga, K. A. See, *ACS Appl. Mater. Interfaces* **2021**, *13*, 18865–18875.
- [23] a) Y. Lu, Z. Tu, L. A. Archer, *Nat. Mater.* **2014**, *13*, 961–969; b) R. Dedryvère, H. Martinez, S. Leroy, D. Lemordant, F. Bonhomme, P. Blensan, D. Gonbeau, *J. Power Sources* **2007**, *174*, 462–468.
- [24] M. He, R. Guo, G. M. Hobold, H. Gao, B. M. Gallant, *Proc. Nat. Acad. Sci.* **2020**, *117*, 73–79.
- [25] J. Mashaiekhy, Z. Shafeizadeh, H. Nahidi, I. Hadi, *Optik* **2013**, *124*, 3957–3961.
- [26] Q. Xu, X. Yang, M. Rao, D. Lin, K. Yan, R. Du, J. Xu, Y. Zhang, D. Ye, S. Yang, G. Zhou, Y. Lu, Y. Qiu, *Energy Storage Mater.* **2020**, *26*, 73–82.
- [27] M. Fuentes, D. de la Fuente, B. Chico, I. Llorente, J. A. Jiménez, M. Morcillo, *Mater. Corros.* **2019**, *70*, 1005–1015.
- [28] a) Q. Ran, H. Zhao, Y. Hu, S. Hao, Q. Shen, J. Liu, H. Li, Y. Xiao, L. Li, L. Wang, X. Liu, *ACS Appl. Mater. Interfaces* **2020**, *12*, 9268–9276; b) J. Wang, Q. Yuan, Z. Ren, C. Sun, J. Zhang, R. Wang, M. Qian, Q. Shi, R. Shao, D. Mu, Y. Su, J. Xie, F. Wu, G. Tan, *Nano Lett.* **2022**, *22*, 5221–5229.
- [29] R. Wang, J. Wang, S. Chen, Q. Yuan, D. Li, X. Zhang, L. Chen, Y. Su, G. Tan, F. Wu, *Nano Energy* **2020**, *76*, 105065.
- [30] C. Yang, H. Xie, W. Ping, K. Fu, B. Liu, J. Rao, J. Dai, C. Wang, G. Pastel, L. Hu, *Adv. Mater.* **2019**, *31*, 1804815.

Manuscript received: May 24, 2022

Revised manuscript received: July 17, 2022

Accepted manuscript online: July 17, 2022

Version of record online: August 3, 2022